

See discussions, stats, and author profiles for this publication at: <https://www.researchgate.net/publication/281456054>

# In Situ Synthesis of MnS Hollow Microspheres on Reduced Graphene Oxide Sheets as High-Capacity and Long-Life Anodes for Li- and Na-Ion Batteries

ARTICLE in ACS APPLIED MATERIALS & INTERFACES · AUGUST 2015

Impact Factor: 6.72 · DOI: 10.1021/acsami.5b06590

---

READS

24

4 AUTHORS, INCLUDING:



Jun Liu

South China University of Technology

78 PUBLICATIONS 3,162 CITATIONS

SEE PROFILE

# In Situ Synthesis of MnS Hollow Microspheres on Reduced Graphene Oxide Sheets as High-Capacity and Long-Life Anodes for Li- and Na-Ion Batteries

Xijun Xu,<sup>†</sup> Shaomin Ji,<sup>\*,†</sup> Mingzhe Gu,<sup>†</sup> and Jun Liu<sup>\*,†,‡</sup>

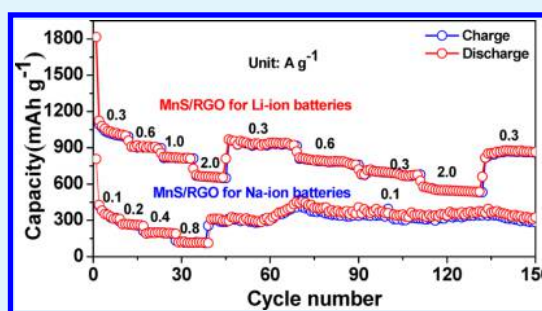
<sup>†</sup>Key Laboratory of Low Dimensional Materials & Application Technology, Ministry of Education, School of Materials Science and Engineering, Xiangtan University, Xiangtan 411105, China

<sup>‡</sup>Key Laboratory of Advanced Energy Storage Materials of Guangdong Province, School of Materials Science and Engineering, South China University of Technology, Guangzhou 510641, China

## S Supporting Information

**ABSTRACT:** Uniform MnS hollow microspheres in situ crystallized on reduced graphene oxide (RGO) nanosheets via a facile hydrothermal method. The MnS/RGO composite material was used as the anode for Na-ion batteries for the first time and exhibited excellent cycling performance, superior specific capacity, and great cycle stability and rate capability for both Li- and Na-ion batteries. Compared with non-encapsulated pure MnS hollow microspheres, these MnS/RGO nanocomposites demonstrated excellent charge–discharge stability and long cycle life. Li-ion storage testing revealed that these MnS/RGO nanocomposites deliver high discharge–charge capacities of 640 mAh g<sup>−1</sup> at 1.0 A g<sup>−1</sup> after 400 cycles and 830 mAh g<sup>−1</sup> at 0.5 A g<sup>−1</sup> after 100 cycles. The MnS/RGO nanocomposites even retained a specific capacity of 308 mAh g<sup>−1</sup> at a current density of 0.1 A g<sup>−1</sup> after 125 cycles as the anode for Na-ion batteries. The outstanding electrochemical performance of the MnS/RGO composite attributed to the RGO nanosheets greatly improved the electronic conductivity and efficiently mitigated the stupendous volume expansion during the progress of charge and discharge.

**KEYWORDS:** MnS/graphene composites, hollow structures, Na-ion batteries, Li-ion batteries, excellent electrochemical performance, anode



## 1. INTRODUCTION

Nowadays, rechargeable Na- and Li-ion batteries are urgently needed for the next generation of energy storage devices because of exhaustion of global fossil-fuel resources and ever-growing environmental problems.<sup>1,2</sup> So, it is imminent to develop electrode materials with low cost, green capabilities, environmentally friendliness, long stable cycling performance, high specific capacity, and high rate capability. The problem that we are faced with right now is developing a high energy density anode material of great urgency because anode materials play a significant role in rechargeable Li- and Na-ion batteries.<sup>3</sup> It is well-known that the traditional graphite material is limited by its theory capacity (372 mAh g<sup>−1</sup> for Li-ion batteries).<sup>2</sup> Transition-metal sulfides with reversible capacities between 500 and 1200 mAh g<sup>−1</sup> have emerged as alternatives to replace traditional graphite-based anode materials.<sup>4–7</sup> Recently, sulfides have attracted intensive attention in the field of energy storage including supercapacitors, solar cells, and Li-ion batteries.<sup>3,8–14</sup> However, because of the large volume dilation involved in the Li<sup>+</sup>/Na<sup>+</sup> uptake and release, the transition-metal sulfide anodes disintegrate, resulting in rapid capacity fade and poor cycling performance. As is known to all, constructing hollow/porous

structures can enhance the cycling performance<sup>4,15–17</sup> because hollow/porous structures with large amounts of cavities provide extra active sites for Li<sup>+</sup>/Na<sup>+</sup> storage, which is a benefit for enhancing the capacity of the electrode materials.<sup>4,9</sup> In addition, this unique hollow structure effectively reduces the diffusion distance of Li<sup>+</sup>/Na<sup>+</sup>.<sup>1,2,17</sup> Furthermore, the hollow/porous structures with larger surface areas would improve the contact between the electrolyte and electrode materials, hence improving the rate capability.<sup>10,16</sup> For example, uniform hollow spheres of CoS<sub>2</sub> have been successfully synthesized via a facile solvothermal method and investigated as anode materials for Li-ion batteries, which exhibited good cycling performance.<sup>18,19</sup> Our research group also successfully synthesized hollow structured LiMn<sub>2</sub>O<sub>4</sub>@LiNi<sub>0.5</sub>Mn<sub>1.5</sub>O<sub>4</sub> and FeF<sub>3</sub>·0.33H<sub>2</sub>O cathode materials, with greatly enhanced cycling performance and rate performance.<sup>20,21</sup>

Reduced graphene oxide (RGO) as a new two-dimensional (2D) carbon material is an ideal substrate for in situ growing and anchoring semiconducting and insulating materials for

Received: July 20, 2015

Accepted: September 3, 2015

energy storage applications because of its high mechanical strength, light weight, high structural flexibility, high chemical stability, high conductivity, and high surface-to-volume ratio.<sup>22–27</sup> The electrochemical performance of various anode materials (e.g., sulfides, oxides, and alloys) can be greatly improved by combining them with RGO.<sup>28–30</sup> Recently, researchers have shown that growing sulfide particles on RGO effectively prevented volume expansion, improved the conductivity and active curves of sulfides/RGO composites, to some extent, and increased the lithium storage capacity and cycling performance of sulfides/RGO composites.<sup>5,31</sup> For example, Xia et al. in situ synthesized  $\text{CoS}_2/\text{RGO}$  nanocomposites with an enhanced electrode performance over pure  $\text{CoS}_2$ .<sup>32</sup> Since the discovery of sulfide materials and because of their successful use in Li-ion batteries, a number of researchers also paid attention to MnS-based materials.<sup>4,33–35</sup> Huang's group synthesized coral-like  $\alpha\text{-MnS}$ , which was embedded in carbon and exhibits a high reversible capacity and good cycling stability for Li-ion batteries.<sup>33</sup> Hollow-structured MnS–carbon nanocomposite powders were synthesized by Kang et al. via a one-pot spray-pyrolysis process and also exhibited good specific capacity and rate capability.<sup>34,35</sup> Difficult yet great progress has been achieved on the MnS-based anodes for Li-ion batteries; the diversities of micro/nanoarchitecture for long-life and high-capacity anode materials based on MnS still need to be greatly expanded to meet ever-developing technology and energy demands. Because the rational design of a hollow structure combined with RGOs can improve their electrochemical performance, herein we successfully in situ synthesized MnS hollow microspheres on 2D RGO nanosheets as superior anode materials for both Li- and Na-ion batteries. Delicate MnS hollow microspheres/RGO composites were successfully prepared through a simple hydrothermal reaction without any template. Most importantly, the MnS hollow microspheres/RGO composites achieved high specific capacity, excellent rate capability, and stable cycling ability, make them promising anode materials for rechargeable Li- and Na-ion batteries.

## 2. EXPERIMENTAL SECTION

### 2.1. Materials Synthesis. 2.1.1. Preparation of Graphite Oxide.

In a typical method synthesis, 5 g of graphite was added to 230 mL of concentrated sulfuric acid in an ice bath along magnetic stirring for 1.5 h, and then 18 g of  $\text{KMnO}_4$  was added under continued magnetic stirring at 35 °C for 1 h until the solution became viscous. The mixture was stirred at 85 °C for another 1 h and diluted with distilled water. A total of 150 mL of 30%  $\text{H}_2\text{O}_2$  was finally added to the solution until the color changed to bright yellow. Finally, graphite oxide was filtered and washed with 5% hydrochloric acid.

**2.1.2. Preparation of Pure MnS Hollow Microspheres.** A total of 3.58 g of a  $\text{Mn}(\text{NO}_3)_2$  solvent with 50 wt % concentration, 2.42 g of L-cysteine, and 0.60 g of urea were added to a beaker under magnetic stirring for 0.5 h to form 200 mL of a mixed solution. Then the solution was transferred into a Teflon-lined stainless steel autoclave and maintained at 160 °C for 24 h. After cooling to room temperature, the precipitate was filtered and washed with distilled water and anhydrous ethanol three times. Then the precursor was dried at 80 °C overnight in a vacuum oven. Finally, the products were annealed at 500 °C for 4 h in nitrogen at a rate of 3 °C  $\text{min}^{-1}$ .

**2.1.3. Preparation of MnS Hollow Microspheres/RGO.** A total of 0.20 g of graphite oxide was added into 200 mL of distilled water and ultrasonicated at 45 kHz for 1 h. Then 3.58 g of a  $\text{Mn}(\text{NO}_3)_2$  solution with 50% concentration, 2.42 g of L-cysteine, and 0.60 g of urea were added to this graphite oxide solution under magnetic stirring for 0.5 h. Then the solution was transferred to a Teflon-lined stainless steel autoclave and maintained at 160 °C for 24 h. After cooling to room

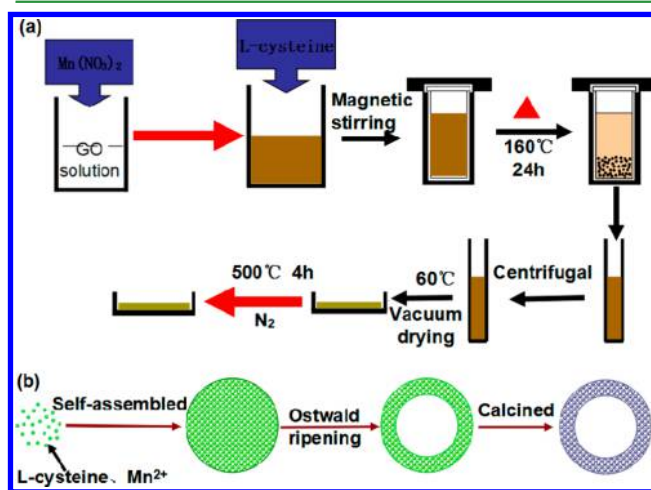
temperature, the precipitate was filtered and washed with distilled water and anhydrous ethanol three times, and then the sample was dried at 80 °C overnight in a vacuum oven. Finally, the products were annealed at 500 °C for 4 h in nitrogen at a rate of 3 °C  $\text{min}^{-1}$ .

**2.2. Materials Characterization.** Scanning electron microscopy (SEM) analysis was performed with a JSM-6610LV scanning electron microscope. High-resolution transmission electron microscopy (HRTEM) analysis was performed with a JEM-2100 microscope. The collected products were characterized by X-ray diffraction (XRD) with a Rigaku-DMax 2400 diffractometer equipped with a graphite-monochromated Cu  $K\alpha$  426 radiation source at a scanning rate of 0.02°  $\text{s}^{-1}$ . Thermogravimetric analysis (TGA) was performed from room temperature to 900 °C at a ramp rate of 10 °C  $\text{min}^{-1}$  with an air flow rate of 20  $\text{mL min}^{-1}$  by using a Q50 thermogravimetric analyzer. The Raman spectra were obtained with a Renishaw Invia Raman microscope. The surface areas of the nanocomposites were measured by the Brunauer–Emmett–Teller (BET) method, using nitrogen as the adsorbate gas.

**2.3. Electrochemical Testing.** The electrochemical performances of the as-prepared products were measured by a charge–discharge test. For preparation of the working electrode, a mixture of MnS/RGO (or pure MnS), acetylene black, and poly(vinylidene fluoride) in a weight ratio of 70:20:10 was ground with *N*-methyl-2-pyrrolidone as the solvent to make slurry. The slurry was then applied to a Cu foil and dried in a vacuum oven at 80 °C for 12 h to form the working electrode. Then the Cu foil was punched into a circular disk with a diameter of 15.8 mm; the active material loading was 1.0–1.5 mg. The test cells (CR2016) were assembled in an argon-filled glovebox ( $\text{H}_2\text{O}$  and  $\text{O}_2 < 0.1$  ppm). A circular Li foil and Na bulk were used as the counter electrodes and Celgard2400 as the separator. A solution of 1 mol of  $\text{LiPF}_6$  in ethylene carbonate/diethyl carbonate (EC/DEC = 1:1 by volume) was used as the Li-ion electrolyte. The Na-ion battery electrolyte was 1 mol of  $\text{NaClO}_4$  dissolved in a mixture of EC/DEC (4:6 by volume). Fluoroethylene carbonate (FEC) was used as the electrode additive. The volume ratio of FEC/EC + DEC is 2%. Galvanostatic discharge and charge at various current densities were performed on a NEWARE-BTS battery tester, with cutoff potentials of 0.01 V for discharge and 2.6 V for charge. The impedance spectra of the cells were also measured with an Electrochemical Workstation (CHI660d) in a frequency from 0.1 Hz to 100 kHz with an alternating-current amplitude of 5.0 mV.

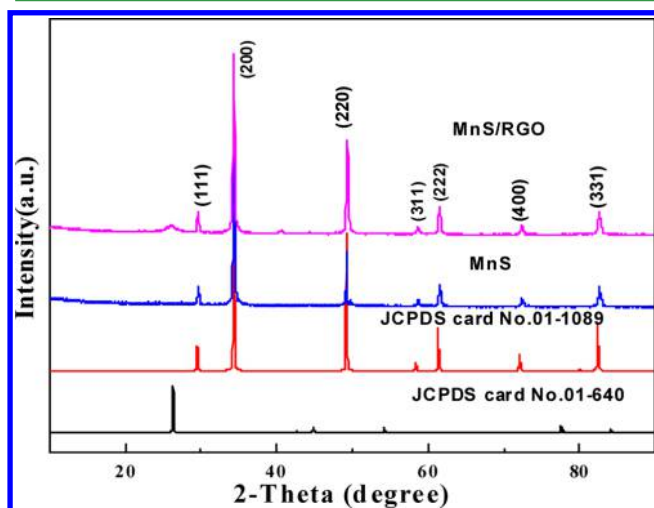
## 3. RESULTS AND DISCUSSION

Figure 1a illustrates the detailed fabrication progress of MnS hollow microspheres/RGO composites. The urea added into



**Figure 1.** Schematics of (a) the experimental process for synthesizing MnS hollow microspheres/RGO composites and (b) of the Ostwald ripening mechanism for forming MnS hollow microspheres.

the solution (in Figure 1a) is to reduce GO and increase the pores in the composite materials. In order to enhance the stability of the MnS hollow microsphere, the composite was finally annealed in nitrogen for 4 h. The formation mechanism of the current hollow-structured MnS microspheres is a typical Ostwald ripening hollowing mechanism (Figure 1b).<sup>21</sup> At the initial stage, a large number of newly formed nanoparticles tend to aggregate into larger particles because of the high surface energy, driven by the surface free energy and self-assembly process, to form a hollow microsphere structure, which is in accordance with the TEM results (Figure 5). Figure 2 shows



**Figure 2.** XRD patterns of pure MnS hollow microspheres and MnS hollow microspheres/RGO composites. The patterns of JCPDS 01-1089 (red curve) and 01-640 (black curve) are also shown.

the XRD patterns of pure MnS microspheres and MnS hollow microspheres/RGO composites, and the dominant diffraction peaks of both MnS and MnS/RGO perfectly matched with the diffraction peaks of JCPDS 01-1089, indicating that the as-prepared MnS can be indexed to cubic MnS (space group  $Fm\bar{3}m$ ). The small diffraction peaks at  $2\theta = 27^\circ$  are well matched with JCPDS 01-640, which is interpreted as RGO in the MnS/RGO composites. From the XRD patterns, we can see that both the as-obtained MnS and MnS/RGO have good crystallinity, ensuring these anode materials good cycling stability during charge–discharge processes.

Figure 3a shows the Raman spectra of both GO and the MnS/RGO composite, revealing two Raman peaks at 1345 and 1587  $\text{cm}^{-1}$  for MnS/RGO and two Raman peaks at 1346 and 1603  $\text{cm}^{-1}$  for GO.

The point area ratio of D band/G band was 0.95 for GO, while the point area ratio of D band/G band was 1.32 for MnS/RGO. This means that through a hydrothermal reaction GO was partly reduced. It is well-known that the D band is related to the vibrations of  $\text{sp}^3$  carbon atoms of defects and disorder in graphite and the G band is linked to the vibrations of  $\text{sp}^2$  carbon atoms and order in graphite.<sup>22–27,31,32</sup> The increased point area ratio of D band/G band is due to the decrease of the average size of the  $\text{sp}^2$  domain and the increase of the number of domains. From these Raman results, it is believed that RGO in reduced MnS/RGO composites with a large number of defects and disordered structure, which would provide more extra sites for  $\text{Li}^+/\text{Na}^+$  storage, thus effectively improves the specific capacity and rate capability. The weight percent of RGO in MnS/RGO composites is further evaluated by TGA. As shown in Figure 3b, the small weight loss below 300  $^\circ\text{C}$  was associated with the absorbed water in MnS/RGO composites. The weight increase between 300 and 500  $^\circ\text{C}$  was related to the formation of  $\text{MnSO}_4$  and  $\text{Mn}_3\text{O}_4$ . The weight loss from 450 to 600  $^\circ\text{C}$  indicated that RGO in MnS/RGO composites was completely burned, and the main weight loss between 700 and 900  $^\circ\text{C}$  was associated with the transformation of  $\text{MnSO}_4$  and  $\text{Mn}_3\text{O}_4$  into  $\text{Mn}_2\text{O}_3$ .<sup>33,34</sup> The exothermic peak in the differential thermogravimetry curve (blue line in Figure 3b) is consistent with the weight loss curve, which corresponds to the chemical reaction and phase transition.<sup>33,34</sup> Through TGA, we found that the weight percent of RGO in MnS/RGO composites was around 24.6%. Such a considerable part of RGO ensures for MnS/RGO a good electronic conductivity and can effectively protect MnS hollow spheres from rupturing during the charge–discharge process.

Parts a–c of Figure 4 show the different-magnification SEM images of pure MnS hollow microspheres. The surface of these microspheres is rough, indicating that these hollow microspheres with large surface area are beneficial for forming a well contact with the electrolyte. The hollow core structure can also provide more extra active sites for  $\text{Li}^+/\text{Na}^+$  storage. It can be observed that part of these hollow microspheres have an open hollow morphology, which would availably reduce the diffusion distance of  $\text{Li}^+$ ,  $\text{Na}^+$ , and electrons. Parts d–f of Figure 4 show the morphology of the MnS/RGO composite, with the MnS particles approximately 1–3  $\mu\text{m}$  in size and each MnS microsphere almost encapsulated with RGO nanosheets. Directly grown electroactive MnS on RGO nanosheets greatly promoted stronger adhesion and improved the electrical conductivity, contributing to the improvement of the electrochemical performance of electroactive MnS. The detailed

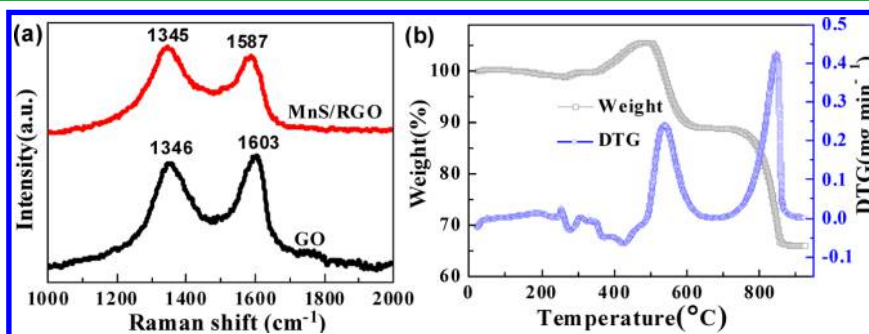


**Figure 3.** (a) Raman spectra of MnS hollow microspheres/RGO (red curve) and GO (black curve). (b) TGA results of hollow MnS microspheres/RGO composites (heated in air with a rate of 10  $^\circ\text{C min}^{-1}$ ).



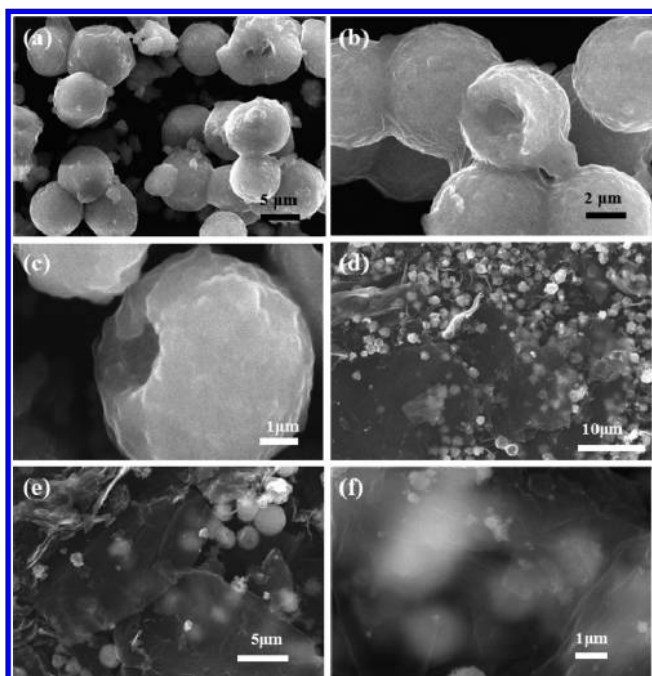


**Figure 4.** Different-magnification SEM image of pure MnS hollow microspheres (a–c) and MnS hollow microspheres/RGO composites (d–f), which show that both electroactive MnS particles have typical hollow cores.

morphology and microstructure information on these pure MnS hollow microspheres and MnS hollow microspheres/RGO composites were further characterized by TEM, as shown in Figure 5. As can be observed from Figure 5a,b, pure MnS has a hollow structure and a rough surface, which is well consistent with SEM observation (Figure 4a–c). As shown in Figure 5c,d, the MnS particles in MnS/RGO composites have a more rugged surface. The electroactive MnS microspheres consist of dense small nanoparticles, self-assembling into a hollow microsphere structure, which is well consistent with the high-magnification SEM images in Figure S1. The lattice spacing of 0.261 nm corresponds to the (200) plane of MnS in both pure MnS hollow microspheres (Figure 5e), and MnS hollow microspheres/RGO composites (Figure 5f) can be clearly observed.

The Li-ion storage performances of these pure MnS hollow microspheres and MnS hollow microspheres/RGO were evaluated by electrochemical impedance spectroscopy (EIS) and galvanostatic charge–discharge cycling using two-electrode coin cells. As shown in Figure 6a–c, the initial discharge specific capacity is much higher than the initial charge specific capacity. The high irreversible capacity in the first large discharge capacity is attributed to the formation of solid electrolyte interface (SEI) and irreversible composition of  $\text{Li}_2\text{S}$ .<sup>36</sup> Although a large irreversible capacity existed in this anode material in the first cycle, the MnS/RGO anodes show an excellent cycling performance and superior capacity retention in the following charge–discharge cycles. As shown in Figure 6a,b, the MnS hollow microspheres/RGO composites exhibit much higher cycling stability than that of pure MnS hollow porous microspheres. At a current density of  $0.3 \text{ A g}^{-1}$ , the initial voltage–specific capacity curves (red curves in Figure 6c) show discharge and charge voltage plateaus at 0.7 and 1.25 V, respectively, which are caused by decomposition of the electroactive MnS into metallic Mn and  $\text{Li}_2\text{S}$  via reaction 1, the

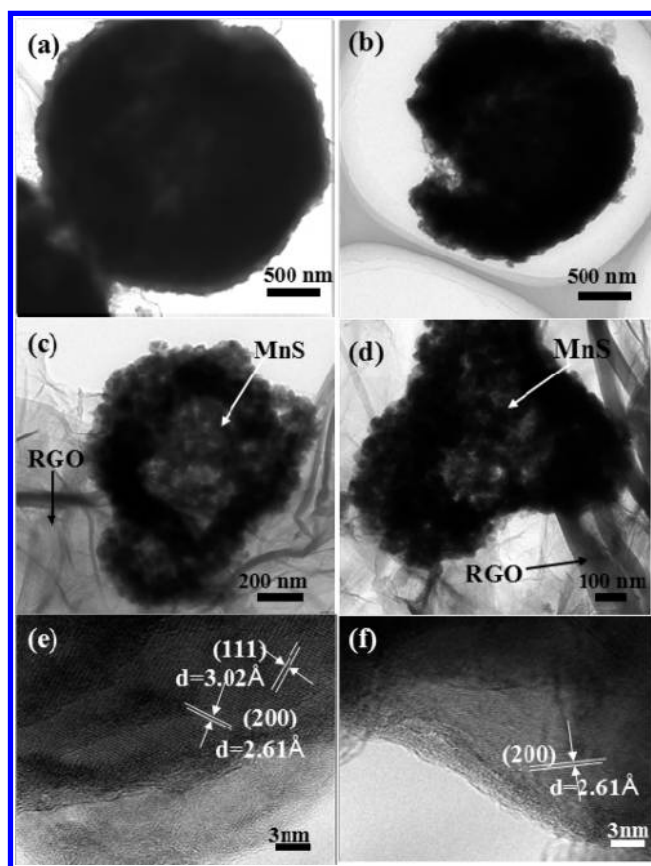
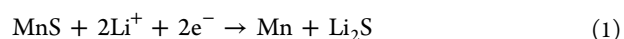


**Figure 5.** TEM characterizations of pure MnS hollow microspheres and MnS hollow microspheres/RGO composites: (a and b) low-magnification TEM images of MnS hollow microspheres; (c and d) low-magnification TEM images of MnS hollow microspheres/RGO composites; (e and f) HRTEM images revealing lattice planes of MnS in pure MnS hollow microspheres (e) and MnS/RGO composites (f).

formation of an SEI and Li-ion insertion into the graphene nanosheets.<sup>31–33</sup>



In Figure 6c, the blue voltage–specific capacity curves show the discharge and charge processes at a current density of  $1.0 \text{ A g}^{-1}$  with voltage plateaus at 0.6 and 1.32 V. When the current density increased to  $2.5 \text{ A g}^{-1}$ , the discharge–charge voltage plateau changed to 0.5 and 1.4 V, as depicted in Figure 6c (black curves). When the charge and discharge current densities of a MnS/RGO composite anode increased, the charge voltage plateau increased and the discharge voltage plateau decayed. This phenomenon occurred as a result of increasing charge and discharge current densities, causing polarization of the active material to become more serious. In the MnS/RGO composite anodes, MnS microspheres with the hollow cavities favor electrolyte flooding and transportation, except the positive effect upon enhancing the electrode performance in terms of both kinetics and the cycling performance.<sup>20</sup> In order to measure Li-ion and electron diffusion of pure MnS and MnS/RGO composites and to explain the different electrochemical performances between MnS and MnS/RGO, EIS plots were made before cycles, as shown in Figure 6d. EIS has been proven to be a useful and important tool for analyzing the dynamics for  $\text{Li}^+/\text{Na}^+$  insertion and extraction of the electrodes.<sup>37–39</sup> Generally, the semicircle

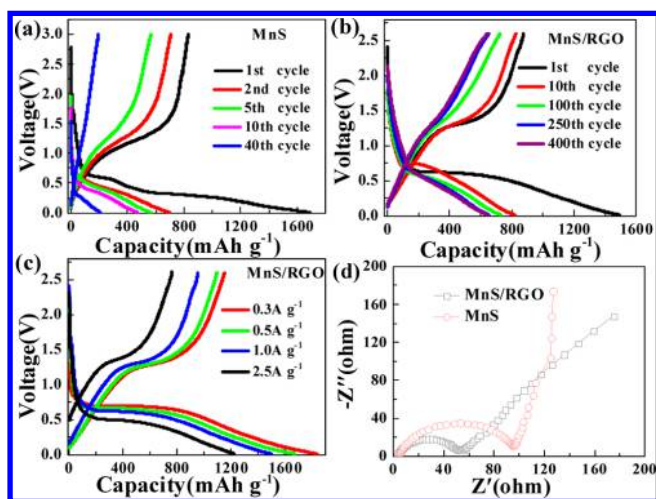


**Figure 6.** Voltage–capacity curves and Nyquist plots of pure MnS hollow microspheres and MnS hollow microspheres/RGO composites for Li-ion batteries: (a) voltage–capacity curves (the 1st, 2nd, 5th, 10th, and 40th) of pure MnS hollow microspheres at a current density of 0.15 A g<sup>-1</sup>; (b) voltage–capacity curves (the 1st, 10th, 100th, 250th, and 400th) of MnS hollow microspheres/RGO composites at a current density of 1.0 A g<sup>-1</sup>; (c) voltage–capacity curves of MnS/RGO anodes at different current densities (increased from 0.3 to 2.5 A g<sup>-1</sup>); (d) Nyquist plots of pure MnS and MnS/RGO composite electrodes obtained by applying a sine wave with an amplitude of 5.0 mV over the frequency range from 0.1 Hz to 100 kHz.

of the impedance in the high-frequency range is related to the diffusion resistance of the Li<sup>+</sup>/Na<sup>+</sup> ion through the SEI membrane.<sup>39,40</sup> The semicircle in the medium-frequency region is associated with the charge-transfer resistance between the active anode materials and the liquid electrolyte.<sup>36</sup> The inclined line in low frequency is attributed to a Warburg-type element reflecting the solid-state diffusion of Li<sup>+</sup>/Na<sup>+</sup> into the bulk of the active materials.<sup>41–44</sup> As shown in Figure 6d, the red curve displays the impedance spectrum of pure MnS hollow microspheres, and the black curve is the impedance spectrum of MnS hollow microspheres/RGO composites. The MnS/RGO composites deliver a smaller resistance than the MnS hollow microspheres, which clearly shows that the introduction of 2D RGO sheets greatly enhanced the electrical conductivity of the MnS electrode. The EIS plots after cycles are displayed in Figure S6 (Supporting Information), also indicating the excellent electrochemical stability of MnS hollow microspheres/RGO composites.

The rate performance and cycling stability of MnS/RGO and MnS anodes for Li-ion batteries are shown in Figure 7 in detail. The pure MnS hollow microspheres show poor capacity retention, while the MnS hollow microspheres/RGO composites display a superior rate performance and great capacity retention. As shown in Figure 7a, the pure MnS microspheres display much worse cycling stability even at a low current density of 150 mA g<sup>-1</sup>. At a higher current of 0.3 A g<sup>-1</sup>, the pure MnS microspheres retain a specific capacity of only 100 mAh g<sup>-1</sup> after 80 cycles, while the MnS hollow microspheres/RGO

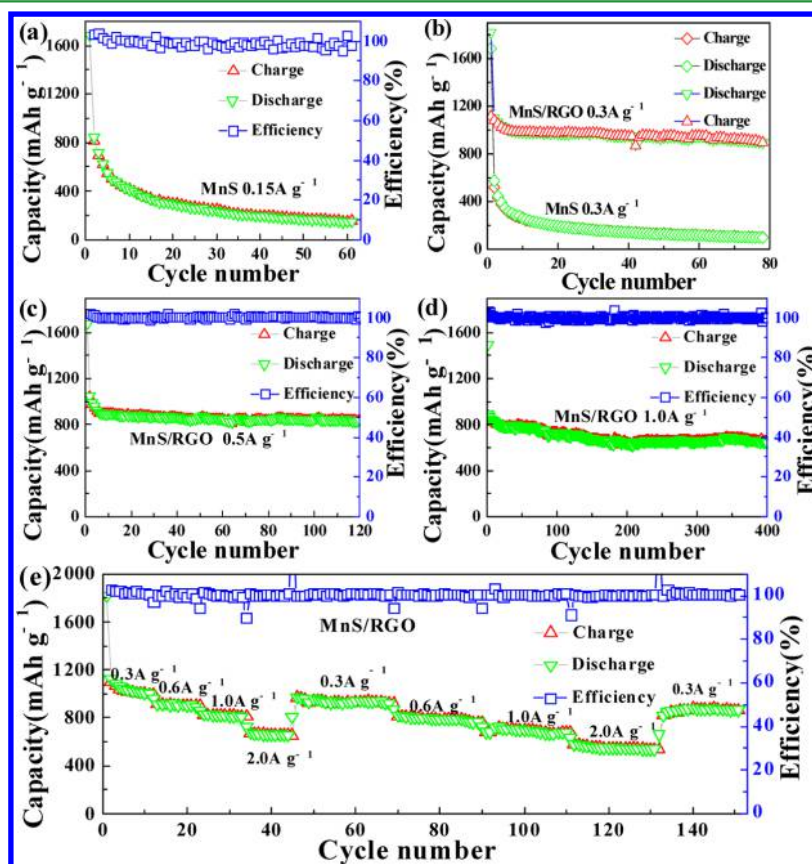


**Figure 7.** Electrochemical performances of pure MnS hollow microspheres and MnS hollow microspheres/RGO composites for Li-ion batteries: (a) cycling performance of pure MnS hollow microspheres at 0.1 A g<sup>-1</sup>; (b) cycling performances of pure MnS and MnS/RGO at 0.3 A g<sup>-1</sup>; (c) cycling stability of MnS/RGO composites at 0.5 A g<sup>-1</sup>; (d) long cycling stability of MnS/RGO composites at 1.0 A g<sup>-1</sup>; (e) rate capability of MnS/RGO composites at different current densities (from 0.3 to 2.0 A g<sup>-1</sup>).



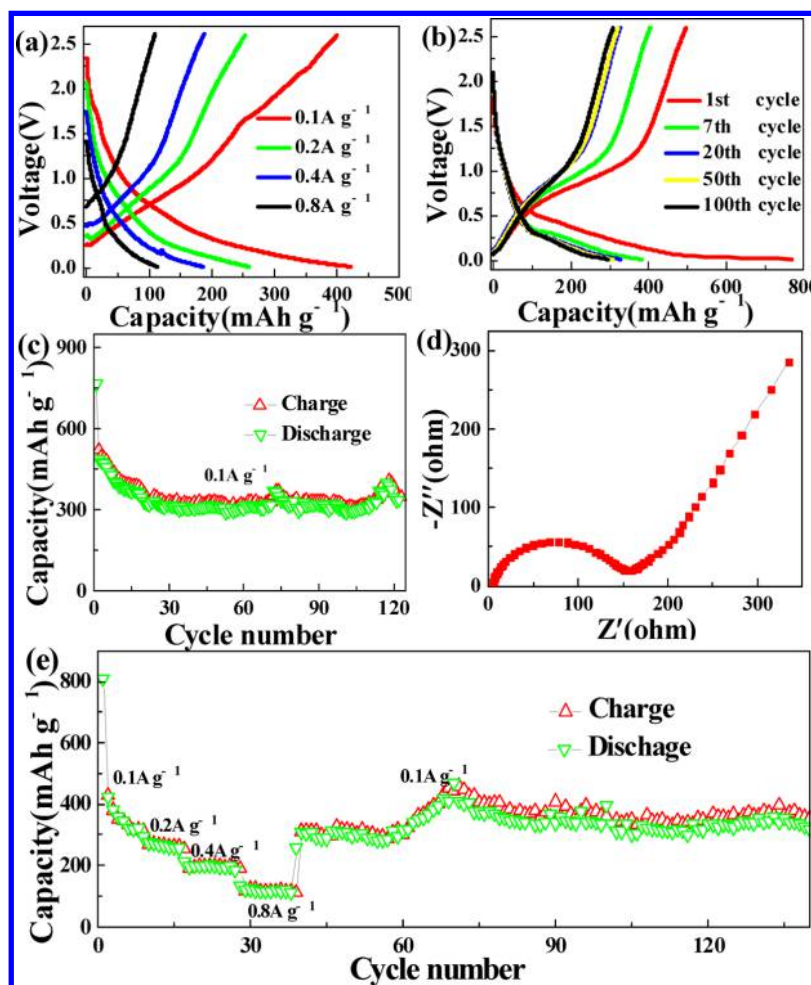
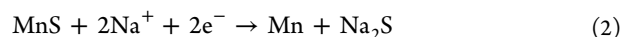


**Figure 8.** Electrochemical performances of MnS hollow microspheres/RGO composites for Na-ion batteries; (a) voltage–capacity curves of the MnS/RGO anode at different current densities (increased from 0.1 to 0.8 A g<sup>−1</sup>); (b) voltage–capacity curves (the 1st, 7th, 20th, 50th, and 100th) of MnS hollow microspheres/RGO composites at a current density of 0.1 A g<sup>−1</sup>; (c) cycle stability of MnS/RGO composites at 0.1 A g<sup>−1</sup>; (d) Nyquist plot of the MnS/RGO composite electrode obtained by applying a sine wave with an amplitude of 5.0 mV over the frequency range from 0.1 Hz to 100 kHz; (e) rate capability of MnS/RGO composites at different current densities (increased from 0.1 to 0.8 A g<sup>−1</sup>).

RGO composites still deliver a high capacity of 900 mAh g<sup>−1</sup> after 80 cycles (Figure 7b). The obvious difference between pure MnS and MnS/RGO owing to the RGO nanosheets evidently improved the electronic conductivity and markedly relieved the volume expansion during the charge–discharge cycles of the MnS/RGO composite. The charge–discharge performance of MnS hollow microspheres/RGO composites were evaluated at different charge currents from 0.3 to 2.0 A g<sup>−1</sup>, as shown in Figure 7e. First, the discharge–charge process was carried out at each charge rate for 10 cycles. Then the current density returned to 0.3 A g<sup>−1</sup> for 35 cycles and 0.5, 1.0, and 2.0 A g<sup>−1</sup> for 20 cycles, respectively. Finally the charge density was reset to 0.3 A g<sup>−1</sup> again. With the current density increased from 0.3 to 2.0 A g<sup>−1</sup>, the specific capacities of the MnS/RGO anode decreased from 1050 to 640 mAh g<sup>−1</sup>. When the current density was first returned to 0.3 A g<sup>−1</sup>, the MnS/RGO anode delivered a specific capacity of about 960 mAh g<sup>−1</sup>. The specific capacity of the MnS/RGO anode decreased from 980 to 580 mAh g<sup>−1</sup> as the current density increased a second time from 0.3 to 2.0 A g<sup>−1</sup>. When the current density was reset a second time to 0.3 A g<sup>−1</sup>, the MnS/RGO anode delivered a specific capacity of 890 mAh g<sup>−1</sup>. The charge–discharge performance of MnS/RGO composites at a current density of

0.5 A g<sup>−1</sup> is depicted in Figure 7c. Even after 100 cycles, MnS hollow microspheres/RGO composites had a high specific capacity of 830 mAh g<sup>−1</sup>. Figure 7d shows the cycling performance of MnS/RGO at a current of 1.0 A g<sup>−1</sup> for 400 cycles, and it is obviously observed that even after 400 cycles the specific capacity of the MnS/RGO material is still 640 mAh g<sup>−1</sup>. The SEM images of MnS/RGO composites after 400 cycles were presented in Figure S4, from which it can be clearly observed that the MnS/RGO anode was still in good condition, strongly supporting their excellent cycling performance.

To estimate the sodium storage ability of MnS hollow microspheres/RGO composites, two-electrode coin-type half-cells were also assembled and a series of electrochemical measurements were carried out at room temperature. The capacity–voltage curves at different current densities (0.1, 0.2, 0.4, and 0.8 A g<sup>−1</sup>) are shown in Figure 8a. The different cycle capacity–voltage curves of the MnS/RGO composite at 0.2 A g<sup>−1</sup> are shown in Figure 8b. As can be seen from this image, the larger discharge capacity than charge capacity can be ascribed to the SEI membrane formation and electrolyte decomposition, which corresponds to the chemical equation (2).<sup>30–34,45</sup>



The Na-ion cell delivers a high irreversible capacity of 497 mAh g<sup>-1</sup> at 0.1 A g<sup>-1</sup> and 308 mAh g<sup>-1</sup> after 125 cycles, as shown in Figure 8c. Such an excellent cycle behavior can be attributed to the RGO nanosheets greatly improving the conductivity of MnS/RGO composites and hollow microspheres effectively reducing the diffusion distance of Na<sup>+</sup>. As shown in Figure 8d, the red curve displays the impedance spectrum of MnS hollow microspheres/RGO composites for Na-ion batteries. The MnS/RGO composite delivers a small resistance, which clearly shows that introducing 2D RGO sheets greatly enhances the electrical conductivity of the MnS electrode. This shows that a larger resistance than that in Li-ion batteries can be associated with Na<sup>+</sup> with a larger radius than Li<sup>+</sup> (Figure S5). The larger radius of Na<sup>+</sup> may be the main factor resulting in Na-ion batteries with smaller capacity than Li-ion batteries, and the different organic electrolytes may also influence the battery capacity.<sup>46</sup> The rate performances at various current densities of 0.1, 0.2, 0.4, and 0.8 A g<sup>-1</sup> delivered average capacities of 350, 265, 180, and 118 mAh g<sup>-1</sup>, respectively, as shown in Figure 8a. When the current density was returned to 0.1 A g<sup>-1</sup>, the cell also delivered a capacity of 365 mAh g<sup>-1</sup>.

The MnS/RGO nanocomposites obtained via an in situ crystallized method exhibited excellent cycling performance, superior rate capability, high coulombic efficiency, and specific capacity. The greatly enhanced electrochemical performance of MnS/RGO was attributed to the unique synthesis method and particular hollow and porous structures of MnS/RGO. MnS microspheres strongly adhered to the 2D RGO because the hollow MnS crystal was in situ grown on the RGO nanosheets, which ameliorate the stability of the MnS/RGO composites. Furthermore, the porous structure of electroactive MnS and encapsulating 2D RGO sheets improved the conductivity of the electroactive materials and reduced the impact for electroactive MnS caused by volume expansion. The unique MnS hollow microspheres/RGO nanocomposites were for the first time used as anode materials for Na-ion batteries and achieved superior capacity and stable rate performance for both Na- and Li-ion batteries.

#### 4. CONCLUSION

In summary, we have successfully in situ synthesized MnS hollow microspheres on 2D RGO sheets via a typical Ostwald ripening process. Such MnS hollow microspheres/RGO composites for both Li- and Na-ion batteries exhibit superior rate capability and cycling performance. The enhanced electrochemical performances could be attributed to their hollow structure and 2D RGO sheet encapsulation. The hollow core structure of MnS reduced the diffusion distance of Li<sup>+</sup>/Na<sup>+</sup>, and the large specific surface area ensured that the material contacted well with the electrolyte solution. Most importantly, the direct growth of electroactive MnS on 2D RGO sheets promoted stronger adhesion and improved the electrical conductivity, contributing to an enhanced electrochemical performance.

#### ■ ASSOCIATED CONTENT

##### ● Supporting Information

The Supporting Information is available free of charge on the ACS Publications website at DOI: 10.1021/acsami.5b06590.

SEM images of MnS microspheres/RGO composites after cycles and of a single MnS microsphere, BET results of MnS microspheres/RGO, cycling performance of a

MnS microspheres/RGO composites anode for Na- and Li-ion batteries, and an electrochemical performance comparison of MnS microspheres/RGO composites with other MnS-based materials (PDF)

#### ■ AUTHOR INFORMATION

##### Corresponding Authors

\*E-mail: smji@xtu.edu.cn.

\*E-mail: jliu@xtu.edu.cn or msjliu@scut.edu.cn.

##### Author Contributions

The manuscript was written through contributions of all authors. All authors have given approval to the final version of the manuscript.

##### Notes

The authors declare no competing financial interest.

#### ■ ACKNOWLEDGMENTS

The authors gratefully acknowledge financial supported from National Natural Science Foundation of China (Grants 11202177 and 51202207).

#### ■ REFERENCES

- (1) Zhu, T.; Peh, N.; Kang, C.; Hong, M.; Ho, G. W. Outside-In Recrystallization of ZnS-Cu<sub>1.8</sub>S Hollow Spheres with Interdispersed Lattices for Enhanced Visible Light Solar Hydrogen Generation. *Chem. - Eur. J.* **2014**, *20*, 11505–11510.
- (2) Liu, J.; Song, K.; van Aken, P. A.; Maier, J.; Yu, Y. Self-Supported Li<sub>4</sub>Ti<sub>5</sub>O<sub>12</sub>-C Nanotube Arrays as High-Rate and Long-Life Anode Materials for Flexible Li-Ion Batteries. *Nano Lett.* **2014**, *14*, 2597–2603.
- (3) Liu, J.; Liu, W.; Chen, K.; Ji, S.; Zhou, Y.; Wan, Y.; Xue, D.; Hodgson, P.; Li, Y. Facile Synthesis of Transition-Metal Oxide Nanocrystals Embedded in Hollow Carbon Microspheres for High-Rate Lithium-Ion-Battery Anodes. *Chem. - Eur. J.* **2013**, *19*, 9811–9816.
- (4) Li, X.; Shen, J.; Li, N.; Ye, M. Fabrication of  $\gamma$ -MnS/rGO Composite by Facile One-Pot Solvothermal Approach for Supercapacitor Applications. *J. Power Sources* **2015**, *282*, 194–201.
- (5) Guo, J.; Li, F.; Sun, Y.; Zhang, X.; Tang, L. Graphene-Encapsulated Cobalt Sulfides Nanocages with Excellent Anode Performances for Lithium Ion Batteries. *Electrochim. Acta* **2015**, *167*, 32–38.
- (6) Zhu, C.; Mu, X.; van Aken, P. A.; Yu, Y.; Maier, J. Single-Layered Ultrasmall Nanoplates of MoS<sub>2</sub> Embedded in Carbon Nanofibers with Excellent Electrochemical Performance for Lithium and Sodium Storage. *Angew. Chem., Int. Ed.* **2014**, *53*, 2152–2156.
- (7) Liu, J.; Wen, Y.; van Aken, P. A.; Maier, J.; Yu, Y. In Situ Reduction and Coating of SnS<sub>2</sub> Nanobelts for Free-Standing SnS@Polypyrrole-Nanobelt/Carbon-Nanotube Paper Electrodes With Superior Li-ion Storage. *J. Mater. Chem. A* **2015**, *3*, 5259–5265.
- (8) Wang, Q.; Jiao, L.; Han, Y.; et al. CoS<sub>2</sub> Hollow Spheres: Fabrication and Their Application in Lithium-Ion Batteries. *J. Phys. Chem. C* **2011**, *115*, 8300–8304.
- (9) Zhang, Z.; Zhao, H.; Zeng, Z.; Gao, C.; Wang, J.; Xia, Q. Hierarchical Architected NiS@SiO<sub>2</sub> Nanoparticles Enveloped in Graphene Sheets as Anode Material for Lithium Ion Batteries. *Electrochim. Acta* **2015**, *155*, 85–92.
- (10) Lee, S. M.; Ko, Y. N.; Choi, S. H.; Kim, J. H.; Kang, Y. C. Capacitive Properties of Reduced Graphene Oxide Microspheres with Uniformly Dispersed Nickel Sulfide Nanocrystals Prepared by Spray Pyrolysis. *Electrochim. Acta* **2015**, *167*, 287–293.
- (11) Liu, J.; Xue, D. Solvothermal Synthesis of CuS Semiconductor Hollow Spheres Based on a Bubble Template Route. *J. Cryst. Growth* **2009**, *311*, 500–503.



- (12) Jin, J.; Zhang, X.; He, T. Self-Assembled CoS<sub>2</sub> Nanocrystal Film as an Efficient Counter Electrode for Dye-Sensitized Solar Cells. *J. Phys. Chem. C* **2014**, *118*, 24877–24883.
- (13) Yang, B.; Zuo, X.; Chen, P.; Zhou, L.; Yang, X.; Zhang, H.; Li, G.; Wu, M.; Ma, Y.; Jin, S.; Chen, X. Nanocomposite of Tin Sulfide Nanoparticles with Reduced Graphene Oxide in High-Efficiency Dye-Sensitized Solar Cells. *ACS Appl. Mater. Interfaces* **2015**, *7*, 137–143.
- (14) Liu, J.; Wen, Y.; Wang, Y.; van Aken, P. A.; Maier, J.; Yu, Y. Carbon-Encapsulated Pyrite as Stable and Earth-Abundant High Energy Cathode Material for Rechargeable Lithium Batteries. *Adv. Mater.* **2014**, *26*, 6025–6030.
- (15) Liu, J.; Zhou, Y.; Liu, C.; Wang, J.; Pan, Y.; Xue, D. Self-assembled Porous Hierarchical-Like CoO@C Microsheets Transformed from Inorganic–Organic Precursors and Their Lithium-Ion Battery Application. *CrystEngComm* **2012**, *14*, 2669–2674.
- (16) Liu, J.; Liu, W.; Wang, Y.; Ji, S.; Wang, J.; Zhou, Y. Facile Synthesis of Layered LiV<sub>3</sub>O<sub>8</sub> Hollow Nanospheres as Superior Cathode Materials for High-Rate Li-Ion Batteries. *RSC Adv.* **2012**, *2*, 10470–10474.
- (17) Liu, J.; Wan, Y.; Liu, C.; Liu, W.; Ji, S.; Zhou, Y.; Wang, J. Solvothermal Synthesis of Uniform Co<sub>3</sub>O<sub>4</sub>/C Hollow Quasi-Nanospheres for Enhanced Lithium Ion Intercalation Applications. *Eur. J. Inorg. Chem.* **2012**, *24*, 3825–3829.
- (18) Wang, Q.; Jiao, L.; Han, Y.; Du, H.; Peng, W.; Huan, Q.; Song, D.; Si, Y.; Wang, Y.; Yuan, H. CoS<sub>2</sub> Hollow Spheres: Fabrication and Their Application in Lithium-ion Batteries. *J. Phys. Chem. C* **2011**, *115*, 8300–8304.
- (19) Su, Q.; Xie, J.; Zhang, J.; Zhong, Y.; Du, G.; Xu, B. In Situ Transmission Electron Microscopy Observation of Electrochemical Behavior of CoS<sub>2</sub> in Lithium-Ion Battery. *ACS Appl. Mater. Interfaces* **2014**, *6*, 3016–3022.
- (20) Liu, W.; Liu, J.; Chen, K.; Ji, S.; Wan, Y.; Zhou, Y.; Xue, D.; Hodgson, P.; Li, Y. Enhancing the Electrochemical Performance of the LiMn<sub>2</sub>O<sub>4</sub> Hollow Microsphere Cathode With a LiNi<sub>0.5</sub>Mn<sub>1.5</sub>O<sub>4</sub> Coated Layer. *Chem. - Eur. J.* **2014**, *20*, 824–830.
- (21) Liu, J.; Liu, W.; Ji, S.; Wan, Y.; Gu, M.; Yin, H.; Zhou, Y. Iron Fluoride Hollow Porous Microspheres: Facile Solution-Phase Synthesis and Their Application for Li-Ion Battery Cathodes. *Chem. - Eur. J.* **2014**, *20*, 5815–5820.
- (22) Li, B.; Rooney, D. W.; Zhang, N.; Sun, K. An In Situ Ionic-Liquid-Assisted Synthetic Approach to Iron Fluoride/Graphene Hybrid Nanostructures as Superior Cathode Materials for Lithium Ion Batteries. *ACS Appl. Mater. Interfaces* **2013**, *5*, 5057–5063.
- (23) Park, S.; An, J.; Jung, I.; Piner, R. D.; An, S. J.; Li, X.; Velamakanni, A.; Ruoff, R. S. Colloidal Suspensions of Highly Reduced Graphene Oxide in a Wide Variety of Organic Solvents. *Nano Lett.* **2009**, *9*, 1593–1597.
- (24) Li, X.; Zhu, Y.; Cai, W.; Borysiak, M.; Han, B.; Chen, D.; Piner, R. D.; Colombo, L.; Ruoff, R. S. Transfer of Large-Area Graphene Films for High-Performance Transparent Conductive Electrodes. *Nano Lett.* **2009**, *9*, 4359–4363.
- (25) Wu, Z.-S.; Zhou, G.; Yin, L.-C.; Ren, W.; Li, F.; Cheng, H.-M. Graphene/Metal Oxide Composite Electrode Materials for Energy Storage. *Nano Energy* **2012**, *1*, 107–131.
- (26) Dreyer, D. R.; Park, S.; Bielawski, C. W.; Ruoff, R. S. The Chemistry of Graphene Oxide. *Chem. Soc. Rev.* **2010**, *39*, 228–240.
- (27) Park, S.; Ruoff, R. S. Chemical Methods for the Production of Graphenes. *Nat. Nanotechnol.* **2009**, *4*, 217–224.
- (28) Kong, S.; Jin, Z.; Liu, H.; Wang, Y. Morphological Effect of Graphene Nanosheets on Ultrathin CoS Nanosheets and Their Applications for High-Performance Li-Ion Batteries and Photocatalysis. *J. Phys. Chem. C* **2014**, *118*, 25355–25364.
- (29) Zhang, S.; Shao, Y.; Liao, H.-g.; Liu, J.; Aksay, I. A.; Yin, G.; Lin, Y. Graphene Decorated With PtAu Alloy Nanoparticles: Facile Synthesis and Promising Application for Formic Acid Oxidation. *Chem. Mater.* **2011**, *23*, 1079–1081.
- (30) Li, H.; Tay, R. Y.; Tsang, S. H.; Liu, W.; Teo, E. H. T. Reduced Graphene Oxide/Boron Nitride Composite Film as a Novel Binder-Free Anode for Lithium Ion Batteries with Enhanced Performances. *Electrochim. Acta* **2015**, *166*, 197–205.
- (31) Xie, J.; Liu, S.; Cao, G.; Zhu, T.; Zhao, X. Self-Assembly of CoS<sub>2</sub>/Graphene Nanoarchitecture by a Facile One-Pot Route and Its Improved Electrochemical Li-Storage Properties. *Nano Energy* **2013**, *2*, 49–56.
- (32) Qiu, B.; Zhao, X.; Xia, D. In Situ Synthesis of CoS<sub>2</sub>/RGO Nanocomposites with Enhanced Electrode Performance for Lithium-Ion Batteries. *J. Alloys Compd.* **2013**, *579*, 372–376.
- (33) Liu, Y.; Qiao, Y.; Zhang, W.-X.; Li, Z.; Hu, X.-L.; Yuan, L.-X.; Huang, Y.-H. Coral-Like  $\alpha$ -MnS Composites with N-Doped Carbon as Anode Materials for High-Performance Lithium-Ion Batteries. *J. Mater. Chem.* **2012**, *22*, 24026–24033.
- (34) Chen, D.; Quan, H.; Wang, G. S.; Guo, L. Hollow  $\alpha$ -MnS Spheres and Their Hybrids with Reduced Graphene Oxide: Synthesis, Microwave Absorption, and Lithium Storage Properties. *ChemPhysChem* **2013**, *78*, 843–851.
- (35) Lee, S. M.; Lee, J. K.; Kang, Y. C. Electrochemical Properties of Hollow-Structured MnS-Carbon Nanocomposite Powders Prepared by a One-Pot Spray Pyrolysis Process. *Chem. - Asian J.* **2014**, *9*, 590–595.
- (36) Aurbach, D.; Levi, M.; Gamulski, K.; Markovsky, B.; Salitra, G.; Levi, E.; Heider, U.; Heider, L.; Oesten, R. Capacity Fading of Li<sub>2</sub>Mn<sub>2</sub>O<sub>4</sub> Spinel Electrodes Studied by XRD and Electroanalytical Techniques. *J. Power Sources* **1999**, *81*, 472–479.
- (37) Chen, J.; Cheng, F. Combination of Lightweight Elements and Nanostructured Materials for Batteries. *Acc. Chem. Res.* **2009**, *42*, 713–723.
- (38) Ma, H.; Zhang, S.; Ji, W.; Tao, Z.; Chen, J.  $\alpha$ -CuV<sub>2</sub>O<sub>6</sub> Nanowires: Hydrothermal Synthesis and Primary Lithium Battery Application. *J. Am. Chem. Soc.* **2008**, *130*, 5361–5367.
- (39) Xu, X.; Ji, S.; Gao, R.; Liu, J. Facile Synthesis of P2-Type Na<sub>0.4</sub>Mn<sub>0.54</sub>Co<sub>0.46</sub>O<sub>2</sub> as a High Capacity Cathode Material for Sodium-Ion Batteries. *RSC Adv.* **2015**, *5*, 51454–51460.
- (40) Liu, J.; Liu, W.; Ji, S.; Wan, Y.; Yin, H.; Zhou, Y. Facile Synthesis of Carbon-Encapsulated Li<sub>4</sub>Ti<sub>5</sub>O<sub>12</sub>@C Hollow Microspheres as Superior Anode Materials for Li-Ion Batteries. *Eur. J. Inorg. Chem.* **2014**, *12*, 2073–2079.
- (41) Wang, L.; Zhao, J.; He, X.; Gao, J.; Li, J.; Wan, C.; Jiang, C. Electrochemical impedance spectroscopy (EIS) study of Li-Ni<sub>1/3</sub>Co<sub>1/3</sub>Mn<sub>1/3</sub>O<sub>2</sub> for Li-ion batteries. *Int. J. Electrochem. Sci.* **2012**, *1*, 345–353.
- (42) Liu, J.; Wan, Y.; Liu, W.; Wang, J.; Zhou, Y.; Xue, D. Advanced Nanostructured Cathode and Anode Materials for High-Performance Li-Ion Batteries. *Energy Environ. Focus* **2012**, *1*, 19–38.
- (43) Li, J.; Xiong, S.; Liu, Y.; Ju, Z.; Qian, Y. Uniform LiNi<sub>1/3</sub>Co<sub>1/3</sub>Mn<sub>1/3</sub>O<sub>2</sub> Hollow Microspheres: Designed Synthesis, Topotactical Structural Transformation and Their Enhanced Electrochemical Performance. *Nano Energy* **2013**, *2*, 1249–1260.
- (44) Zhang, L.; Zhou, L.; Wu, H. B.; Xu, R.; Lou, X. W. D. Unusual Formation of Single-Crystal Manganese Sulfide Microboxes Co-mediated by the Cubic Crystal Structure and Shape. *Angew. Chem. Int. Ed.* **2012**, *124*, 7379–7382.
- (45) Shadike, Z.; Cao, M.-H.; Ding, F.; Sang, L.; Fu, Z. Improved Electrochemical Performance of CoS<sub>2</sub>/MWCNT Nanocomposites for Sodium-Ion Batteries. *Chem. Commun.* **2015**, *51*, 10486–10489.
- (46) Liu, J.; Wen, Y.; van Aken, P. A.; Maier, J.; Yu, Y. Facile synthesis of highly porous Ni-Sn intermetallic microcages with excellent electrochemical performance for lithium and sodium storage. *Nano Lett.* **2014**, *14*, 6387–6392.